NNT : ***

n°LAL : ***

Characterisation of SuperNEMO demonstrator calorimeter timing performance
Study of 208Tl background rejection influence on the 0nubb decay sensitivity

Thèse de doctorat de l'Université Paris-Saclay
préparée à l'Université Paris Saclay au sein du Laboratoire Irène-Joliot Curie
(anciennement Laboratoire de l'Accélérateur Linéaire)

École doctorale n°576 Particles, Hadrons, Energy, Nuclei,
Instrumentation, Imaging, Cosmos et Simulation (PHENIICS)
Spécialité de doctorat : Physique des particules

Thèse présentée et soutenue à Orsay, le 11 décembre 2020, par

CLOÉ GIRARD-CARILLO

Composition du Jury :

Alessandra Tonazzo APC - Paris	Rapporteure
Mark C. Chen Queen's University	Rapporteur
Christine Marquet CENBG - Bordeaux-Gradignan	Examinatrice
Achille Stocchi LAL - Orsay	Examinateur
Laurent Simard LAL - Orsay	Directeur de thèse
Mathieu Bongrand LAL - Orsay	Co-directeur de thèse

Thèse de doctorat

Contents

Acknowledgement 3

Contents 5

Introduction 9

1 Phenomenology of particle physics 11
- 1.1 The Standard Model of particle physics . . . 11
  - 1.1.1 Bosons . . . 11
  - 1.1.2 Fermions . . . 11
  - 1.1.3 $2\nu\beta\beta$ decay . . . 11
  - 1.1.4 Where the Standard Model ends . . . 11
- 1.2 Going beyond the Standard Model with neutrinos . . . 11
  - 1.2.1 Neutrino flavors and oscillations . . . 11
  - 1.2.2 Neutrino masses and nature . . . 11
  - 1.2.3 Neutrinoless double beta decay . . . 11
  - 1.2.4 Other searches beyond the Standard Model with neutrinos . . . 11
- 1.3 $0\nu\beta\beta$ experiment status . . . 11
  - 1.3.1 Experimental design criteria . . . 11
  - 1.3.2 $0\nu\beta\beta$ direct search experiments . . . 13
  - 1.3.3 Bolometers . . . 14
  - 1.3.4 Time projection chambers . . . 14
  - 1.3.5 Scintillators . . . 15
  - 1.3.6 Tracking calorimeters . . . 17

2 The SuperNEMO demonstrator 19
- 2.1 The SuperNEMO technology . . . 20
  - 2.1.1 Detection principle . . . 20
  - 2.1.2 The source foils . . . 22
  - 2.1.3 The tracker . . . 25
  - 2.1.4 The calorimeter . . . 29
  - 2.1.5 The magnetic coil and the shieldings . . . 34
  - 2.1.6 Calibration strategy . . . 35

2.1.7 Detector cabling . . . 37
2.1.8 Electronics . . . 39
2.1.9 Detector gas tightness . . . 42
2.2 Backgrounds . . . 44
2.2.1 Internal background . . . 44
2.2.2 External background . . . 46
2.2.3 Radon background . . . 47
2.2.4 Background reduction . . . 48
2.3 The SuperNEMO software . . . 48
2.3.1 Simulation . . . 49
2.3.2 Reconstruction pipeline . . . 49
2.3.3 Analysis tools . . . 50
2.4 Conclusion . . . 53

3 Sensitivity of the SuperNEMO demonstrator to the $0\nu\beta\beta$ 55
3.1 The $0\nu\beta\beta$ signal and background model . . . 55
3.1.1 The $0\nu\beta\beta$ signal . . . 56
3.1.2 Inside detector backgrounds . . . 56
3.1.3 External backgrounds . . . 57
3.1.4 Expected number of decays . . . 58
3.2 Event selection . . . 59
3.2.1 Electron definition . . . 59
3.2.2 Total energy spectrum . . . 59
3.3 Demonstrator sensitivity to the $0\nu\beta\beta$ decay of ^{82}Se . . . 61
3.3.1 Sensitivity to the $0\nu\beta\beta$ half-life . . . 61
3.3.2 Limit on the effective neutrino mass . . . 63
3.4 Impact of sources contamination levels on the sensitivity . . . 65
3.4.1 Contamination levels . . . 65
3.4.2 Optimisation of event selection . . . 68
3.5 Impact of the magnetic field on the sensitivity . . . 74
3.5.1 Simulations of the magnetic field inside the demonstrator and reconstructed track fit . . . 74
3.5.2 Impact of the magnetic field on signal and background selections . . . 75
3.5.3 Influence of the magnetic field on optical modules and reconstruction efficiency . . . 77
3.5.4 Simulations with a non-uniform magnetic field . . . 78
3.6 Searching for the Neodymium-150 $0\nu\beta\beta$ decay . . . 80
3.6.1 Searching for the $0\nu\beta\beta$ of other isotopes . . . 80
3.6.2 Sensitivity to the $0\nu\beta\beta$ of ^{150}Nd . . . 80
3.7 The final detector sensitivity . . . 82
3.8 Conclusion . . . 83

4 Improvement of the internal Thallium-208 background rejection 87
4.1 Motivations . . . 87
4.2 The internal ^{208}Tl background . . . 88
4.2.1 The internal conversion process . . . 89

4.2.2 ^{208}Tl disintegrations in the 2e channel . . . 90
4.3 Simulated demonstrator performances . . . 90
4.4 Rejection of ^{208}Tl with a time-of-flight criterion . . . 92
4.4.1 The internal probability . . . 92
4.4.2 The exponential probability for ^{208}Tl events . . . 94
4.5 Event selection . . . 97
4.5.1 Energy selection . . . 97
4.5.2 Time-of-flight cut-off . . . 97
4.5.3 Probability cut-off . . . 99
4.5.4 Influence of the calorimeter time resolution . . . 102
4.6 Impact of ^{208}Tl rejection on the experiment's sensitivity . . . 103
4.6.1 Sensitivity results . . . 105
4.6.2 Expected number of background . . . 107
4.7 Conclusion . . . 108

5 Calorimeter commissioning 109
5.1 Optical modules calibration . . . 109
5.1.1 Pulse shape studies . . . 109
5.1.2 Baseline studies . . . 110
5.1.3 Gain studies . . . 110
5.1.4 Energy calibration . . . 111
5.2 Light Injection System . . . 112
5.3 Calorimeter cabling network . . . 114
5.3.1 Motivations . . . 114
5.3.2 Experimental setup . . . 115
5.3.3 Pulse shape analysis . . . 116
5.3.4 Pulse timing . . . 118
5.3.5 Signal attenuation . . . 123
5.3.6 Conclusion . . . 124
5.4 Synchronisation of calorimeter FEBs . . . 125
5.5 Conclusion . . . 127

6 Characterisation of the calorimeter time resolution 129
6.1 Interaction of particles in the SuperNEMO scintillators . . . 130
6.1.1 Interaction of electrons . . . 130
6.1.2 Interaction of photons . . . 130
6.2 Measurement of the time resolution with a ^{60}Co source . . . 131
6.2.1 Time response of optical modules . . . 132
6.2.2 Description of ^{60}Co nucleus . . . 134
6.2.3 Experimental design . . . 135
6.2.4 Signal events selection . . . 137
6.2.5 Energy calibration . . . 139
6.2.6 Background estimation . . . 142
6.2.7 Determination of the individual timing resolution of each optical module . . . 145
6.2.8 Improvement of the method . . . 149
6.2.9 Conclusion . . . 149

6.3 The Light Injection System 150
6.3.1 Light injection system commissioning 150
6.3.2 Time resolution of optical modules 150

Conclusion **151**

Résumé **153**

Bibliography **155**

CHAPTER 6

Characterisation of the calorimeter time resolution

The precise knowledge of the different particle interaction times in the optical modules of the SuperNEMO calorimeter is important to better understand and reject the background. For example, the study of electron time-of-flight allows us to distinguish internal events (occurring within the source foils) from external events (radioactive decays occurring outside the source foils, for example in the PMTs or in the iron shielding).

During the commissioning phase, a lot of work, presented in the previous chapter, was achieved to calibrate the detector. Following on from this task and completing it, a great part of my PhD was allocated to determine the time resolution of the SuperNEMO calorimeter, and to provide tools to the collaboration to purchase this analysis.

In this chapter we present different studies conducted in order to characterise the time response of the SuperNEMO optical modules. Although the goal of the presented studies is to characterise the time resolution of the SuperNEMO calorimeter, some detector adjustments were still ongoing at the time of the acquisition, that could influence the presented results. Especially, the energy calibration described in Sec. 5.1.4 was not complete, and the Light Injection System presented in Sec. 6.3 was not yet fully operational. However, all the work presented here is necessary in the framework of the first calorimeter calibration. Moreover, I provide all the analysis tools for the collaboration, with a view to doing a possible update, once the whole demonstrator calibration will be achieved.

The first study presented in this chapter focuses on the characterisation of the time resolution of the SuperNEMO calorimeter, using a calibration source made of ^{60}Co. In the second part of this chapter, we study the possibility to gather informations on the calorimeter time resolution using the Light Injection System, a set-up initially designed to calibrate in energy the calorimeter.

6.1 Interaction of particles in the SuperNEMO scintillators

Understanding how particles interact in the SuperNEMO scintillators is essential. The calorimeter part of the demonstrator mainly aims to detect electrons and photons. In this section, we review ***.

6.1.1 Interaction of electrons

Electrons interact with matter through one of two processes: elastic scattering on a nucleus, or inelastic scattering on an atomic electron. Inelastic scatterings are dominant for polystyrene scintillators and occur through two different forms: coherent scattering with the electron cloud, and radiative energy losses (the so-called bremsstrahlung effect). In Fig. 6.1a is displayed the stopping power of electrons in polystyrene for these two processes. Electrons detected in the SuperNEMO calorimeter should deposit a minimal energy of 50 keV (the acquisition low energy threshold) and a maximal energy of few MeV (depending on the $2\nu\beta\beta$ isotope). In this energy range, collisions with the electron cloud are preponderant compared with radiative energy losses. In Fig. 6.1b, we give informations about the mean free path of an electron in polystyrene. In particular, we observe that an electron of 1 MeV penetrates, on average, several millimetres into a polystyrene scintillator.

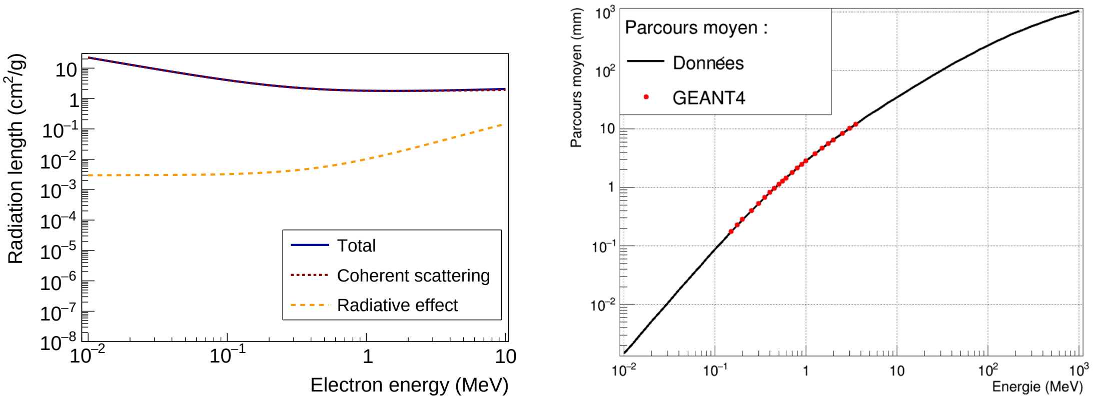

(a)

(b)

Figure 6.1: Stopping power (a) and mean free path (b) for electrons in polystyrene. (a) Energy losses through radiative effect (orange dashed line) and coherent scattering (red dashed line), which is the dominant process for the considered energy range [29]. (b) At 1 MeV, the mean free path of an electron is about 3 mm. Adapted from [15].

6.1.2 Interaction of photons

Photons travelling in matter can interact with the electronic cloud, through three main processes, whose contributions are presented in fig. 6.2a, depending on their energies. Low-energy photons mainly interact with the electron cloud, either

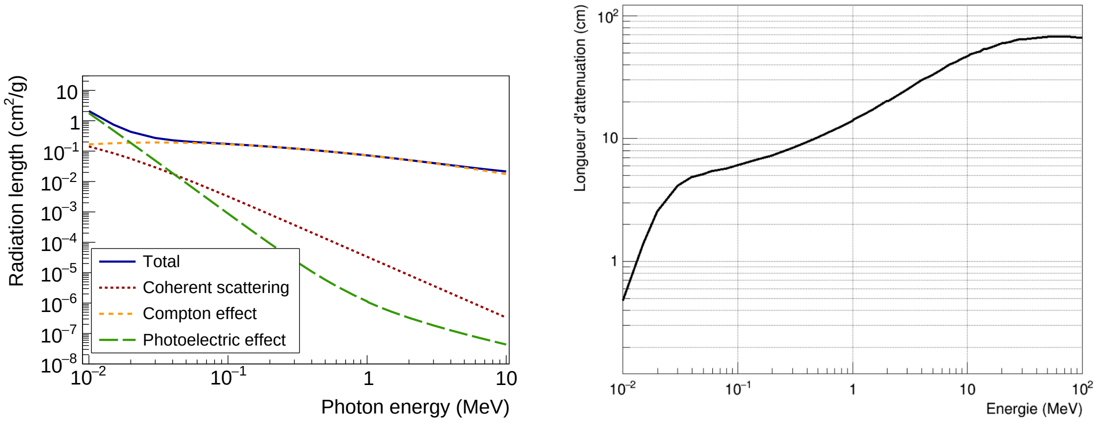

(a) (b)

Figure 6.2: Linear attenuation coefficient (a) and attenuation length (b) for γ radiations in a plastic scintillator made of polystyrene. (a) In the considered energy range of 10 keV – 10 MeV, γ radiations interact with matter mainly through Compton diffusion [30]. (b) The attenuation length of a γ radiation is about 10 cm at 1 MeV. Adapted from [15].

through photoelectric effect (γ radiation is fully absorbed by an electron of the cloud), or through coherent (so-called Rayleigh) scattering. But the dominant effect, for energies between 10 keV and 10 MeV, is the Compton inelastic scattering of a γ with an atomic electron. In Fig. 6.2b, we display the mean attenuation length of a γ radiation in polystyrene scintillators, with energy. Thus, most of 1 MeV γ radiations will interact around 10 cm inside the scintillating material.

At the considered energy range (10 keV – 10 MeV), the interaction of photons with matter is dominated by Compton effect, while the electrons interact mainly through coherent scattering. The SuperNEMO scintillators are designed to detect such particles. Photons have a high probability to interact inside the volume of the scintillator, while electrons are stopped in the first few millimetres.

The following section are devoted to the study of the time resolution of the SuperNEMO optical modules.

6.2 Measurement of the time resolution with a ^{60}Co source

This section is dedicated to detail the time resolution study performed using a ^{60}Co source, exploiting the time characteristic of two photons emitted during the radioactive disintegration process of this nucleus. A great proportion of the whole SuperNEMO demonstrator was successfully characterised using this radioactive source.

6.2.1 Time response of optical modules

In order to characterise the energy and time-of-flight of incoming particles (photons, electrons), each calorimeter block of SuperNEMO is composed of a scintillator and a photomultiplier. As detailed in Chapter 2, the purpose of the scintillator material is to stop the incoming particles, which will induce the production of the so-called optical photons. The optical photons reaching the photomultiplier photocathode are then converted into electrons, with an efficiency called quantum efficiency. After amplification, electrons are collected by the anode which delivers an electric signal whose charge proportional to the initial amount of incident photoelectrons. This signal is then transmitted, via the PM voltage divider, to the electronic readout, where the signal is sampled. The particle energy, as well as the time-of-flight, can be extracted from the signal waveform analysis. Each step of the particle detection process, from the incident particle interaction inside the scintillator, to the signal sampling at the electronic readout, can have an impact on the precise time measurement of the charged particle. In Chapter 2 and 4 we introduced the so-called calorimeter time resolution σ_t, which encapsulates the global uncertainty on the time-of-flight measurement of particles into the calorimeter (Eq. (2.5)). The squared time-resolution can therefore be expressed as the sum of two contributions: the scintillator resolution $\sigma^2_{t,\mathrm{sc}}$, and the PMT resolution $\sigma^2_{t,\mathrm{PM}}$,

$$\sigma_t^2 = \sigma^2_{t,\mathrm{sc}} + \sigma^2_{t,\mathrm{PM}} \,. \tag{6.1}$$

In the following, we detail in depth the physical origins of these terms.

Scintillator time dispersion

The scintillator temporal dispersion $\sigma_{t,\mathrm{sc}}$ in Eq. (6.1) receives contributions mainly from two important characteristics of the scintillator operating principle.

Interaction point: The incoming particle's interaction point location inside the scintillator block highly contributes to the scintillator temporal uncertainty, and depends on the incident particle type. In fact, this effect will not have the same impact on time dispersion, depending on whether the incident particle is a photon or an electron. In Fig 6.3 are schemed the interactions of a photon and that of an electron for the specific case of a SuperNEMO plastic scintillator. In Sec. 6.1, we exposed the different interaction types of photons and electrons. We have also explained the origin of the differences that exist in terms of interaction depth between these two types of particles. To remain consistent with these conclusions, we represent the electron as interacting in the first millimetres, while the photon stops deep inside the scintillator. When a particle (photon or electron) interacts in the scintillating material, the absorbed energy leads to the isotropic emission of scintillation photons: they propagate inside the scintillator, in all directions from the interaction point, at the speed of c/n_{sc}, with n_{sc} the optical index of polystyrene, and c the light speed in vacuum. Depending on their initial direction, some of those photons propagate straight to the PMT (we name them the *direct* photons), while others are at least reflected once on the scintillator surface, before

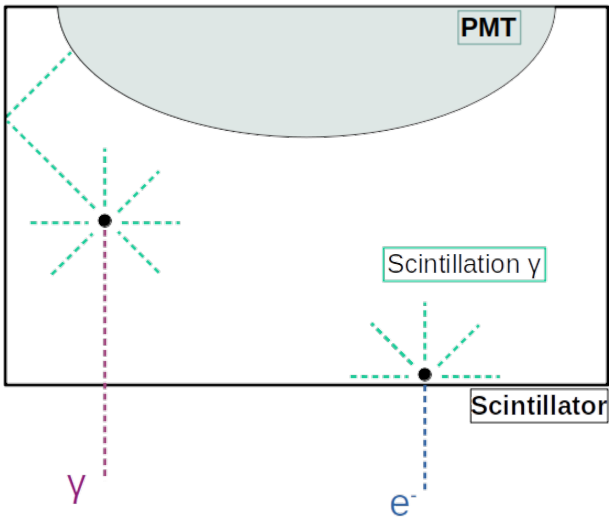

Figure 6.3: A scheme of interaction of particles in a scintillator. The photon case is displayed on the left in pink dotted line, and the electron case is on the right in dark blue dotted line. Both particles enter in the scintillator through the front face. Examples of interaction points inside the scintillator are represented by the black dots. The photons of scintillation emitted isotropically after the interaction are materialised by the bright green dotted lines. Due to different interaction probabilities in matter, the two particles intercat at different depths inside the scintillator. The photon can interact deeply inside the volume, while the electron has a high probability to stop within the first few millimetres.

reaching the PM glass. This mechanism leads to time delays between direct and reflected photons.

In order to illustrate, and give an order of magnitude of this delay, let us consider an example where an incoming electromagnetic particle enters a scintillator from the front face, and interacts right in the centre of the scintillator volume. After the scintillation emission process, a direct photon will reach the PM glass surface at time

$$t_s = \frac{L}{2c/n_{sc}}\,, \tag{6.2}$$

L being the scintillator width. Now, let us consider another photon, that we name *backward reflected*, emitted in the opposite direction. It will propagate, reflect on the front scintillator surface, and finally reach the PM at

$$t_r = \frac{3L}{2c/n_{sc}}\,. \tag{6.3}$$

This reflected photon is therefore delayed compared to the direct photon, with a time-shift of

$$\Delta t^{r,s} = t_r - t_s = \frac{L}{c/n_{sc}}\,. \tag{6.4}$$

In the case of a SuperNEMO scintillator, the length L has been designed to 25 cm, and the optical index is the one of polystyrene with $n_{sc} = 1.5$. Finally, for an incoming particle interacting at the centre of a SuperNEMO scintillator volume, a backward reflected scintillation photon will reach the PM glass 1.25 ns later than a direct photon. And this delay is even more important as the incident particle interacts deep inside the scintillator.

In view of the conclusions given in Sec. 6.1, we know that photons have a higher probability of interacting far into the scintillator block, compared with electrons. Therefore, this time-shift effect is all the more important for incoming photons, while it is quite negligible for incoming electrons, for which reflected photoelectrons reach the PM glass almost as the same time as the direct ones.

This mechanism increases the signal collection rising time at the PM anode, and boosts the scintillator time dispersion $\sigma_{t,\mathrm{sc}}$, with $\sigma_{t,\mathrm{sc}}^{\gamma} > \sigma_{t,\mathrm{sc}}^{\mathrm{e}^-}$.

Scintillating light emission: When a particle interacts in a SuperNEMO scintillator, two successive mechanisms of light absorption/re-emission take place. Firstly, the excitation of scintillator molecules leads to the creation of fluorescence photons. Afterwards, those optical photons are absorbed, then re-emitted by the POPOP agent, at higher wavelengths. The characteristic times of these two processes contribute to increase the scintillator time dispersion $\sigma_{t,\mathrm{sc}}$.

Photomultiplier time dispersion

A photomultiplier is a photodetector: after the light is collected and converted at the photocathode, the photoelectrons are multiplied. The transit time for the photoelectrons emitted at the photocathode to reach the anode after being multiplied is not constant for every photoelectron, due to a varying path for electrons emitted by the different dynodes. This results in a timing dispersion. This fluctuation is called transit time spread (TTS). It leads to an uncertainty on the time measurement and so has an influence on the photomultiplier time dispersion $\sigma_{t,\mathrm{PM}}$.

As discussed in Chapter 4, the time uncertainty brought by the scintillator light emission process and the photomultiplier was characterised for each optical module before the calorimeter assembly. It is possible that the optical modules time resolutions may have changed during the phases following their measurement, so they must be measured again. To do so, data acquisitions were taken with the calorimeter, behind which a ^{60}Co calibration source was set, allowing to detect the two emitted γ's.

6.2.2 Description of ^{60}Co nucleus

The ^{60}Co is a man-made isotope, with a 5.27 years half-life, of which we provide the main interesting properties in the simplified decay scheme of Fig. 6.4. This unstable nucleus spontaneously decays, through the β^- process, into an excited state of Nickel 60. To reach the ground state of the Nickel 60, the nucleus goes through two successive energy levels, emitting in 99.83% of the cases two photons of 1.17 MeV and 1.33 MeV, respectively. The life-time of the second energy level is under the picosecond, thus very short with respect to the expected timing precision of the calorimeter. Therefore, the two photons are considered as emitted in coincidence.

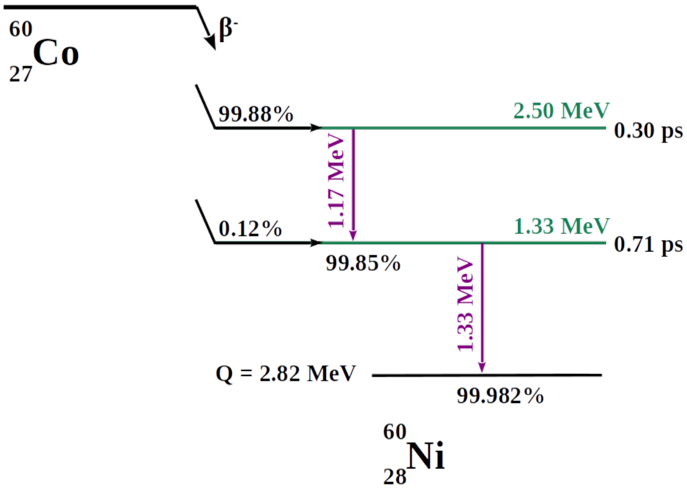

Figure 6.4: A simplified decay scheme for ^{60}Co [31]. The Cobalt decays, through β^-, predominantly to the 2.50 MeV state. Then, two succesive γ's (whose energy levels are represented in green) are emitted in 99.83% of the cases. The two photons have an energy of 1.17 MeV and 1.33 MeV, respectively. As the life-time of the 1.33 MeV energy level is short (< 1 ps) with respect to the timing precision of the calorimeter, the two photons can be considered as emitted in coincidence. We use this property to calibrate in time the demonstrator optical modules.

We aim to detected these two photons and look for coincidences between pairs of optical modules to determine their time resolution.

6.2.3 Experimental design

The idea to use a ^{60}Co source to characterise the time response of the calorimeter part of SuperNEMO had never been tested before the current analysis. Therefore, all the experimental design had to be implemented.

Setting up the experimental design

The initial activity of the Cobalt source we used for this experimental set-up was 447.4 kBq in February 2014. Given the half-life of this isotope, it was reduced to 232 kBq at the time of the data-taking. In order to determine the best design, and later to monitor and compare the results obtained in the framework of this analysis, I performed simulations of ^{60}Co disintegrations for the demonstrator configuration. The characteristics of those simulations are detailed later in this section.

As described in Chapter 2, the SuperNEMO calorimeter is composed of two main walls (called *French* and *Italian* sides), as well as the so-called X-Walls (on the detector sides) and γ-Vetos (on top and below the detector). At the time of the data-taking, X-Walls and γ-Vetos were not yet operational, hence the current analysis only applies on the French and Italian main calorimeter walls. As the demonstrator was closed at this time, it was impossible to set the Cobalt source inside the detector, at the source foils level. Hence, the calibration source was placed behind the calorimeter, as displayed in Fig. 6.5, where sketches of side and back views of the calorimeter are drawn. In order for all PMs to detect

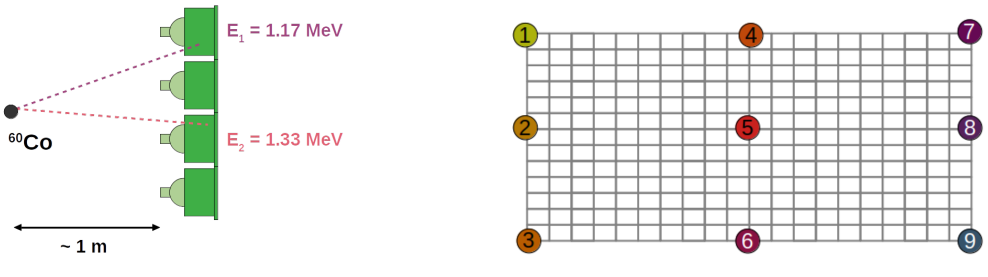

(a) (b)

Figure 6.5: (a) Side view example of the Cobalt source positioning behind a calorimeter main wall, schemed by 4 optical modules (green). The emissions of the 2 γ's of interest are displayed in coloured dotted lines. (b) Back view of the nine source positions behind a main wall. Each grey box represents an optical module.

γ's from Cobalt decays, several bunches of data acquisitions were taken: the source was placed at 9 different positions on each of the 2 main calorimeter walls, approximately one meter behind. Therefore, in total, 19 data acquisitions have been taken, of which:

- 18 with the Cobalt source set behind the wall. The 9 different positions for one wall are represented in Fig. 6.5b.
- 1 acquisition have been taken without the Cobalt source, with the Italian main wall, to characterise the background detected with the current calorimeter settings.

Each data acquisition lasted about 25 minutes, for a total of 10 hours of on-site activities, taking into account the time needed to move the Cobalt source from spot to spot.

Currently, the demonstrator is not protected from the laboratory lights by the anti-radon tent. As laboratory lights would damage the SuperNEMO photomultipliers under tension, two removable black curtains are deployed on top of the detector (that do not interfere with data collection), and acquisitions are taken in dark laboratory. With this way of doing, all data acquisitions can be performed, while eventual necessary repairs remain possible during the detector commissioning.

Taking acquisitions in the dark is a big constraint. Moreover, the Cobalt source, initially used for teaching purposes, was loan by IPN laboratory (Orsay), for only two weeks, mainly because of legal constraints. Therefore, to not disturb LSM on-site activities by plunging the whole laboratory into darkness, and to make the loan time profitable, a SuperNEMO team and I performed night shifts to take data. The acquisition took place during two weeks, at the summer break 2019.

Simulations and analysis pipelines

As for the data acquisition, the simulated source has been placed behind the calorimeter walls. Hopefully, there was no need to simulate all the 18 positions. In fact, at this time, the detector implemented in simulations is symmetrical in terms of detection performances. Therefore, simulations of ^{60}Co events behind the two main walls are equivalent, and we only need to simulate events from 4 locations (positions 1, 2, 4 and 5, according to the Fig. 6.5b numbering system), other being obtained by symmetry operations. Four bunches, for a total of 10^9 Cobalt events, were simulated with the official Falaise pipeline and stored at the IN2P3 computing centre platform, making them available to the collaboration.

As the objective is to determine the optical modules time resolution, σ_t, due to the scintillator light emission process and to the photomultiplier, all simulations were performed with an ideal calorimeter, setting up $\sigma_t = 0$ ps. In that case, the only remaining contribution of optical modules to the time resolution is geometrical and comes from the interaction point uncertainty inside the scintillator. The idea behind that is to compare simulated and real data in order to bring out the contribution of σ_t to the total calorimeter time uncertainty.

The entire experimental set-up was designed and carried out by me and a group of physicists from LAL, Orsay and LPC, Caen. I developed a complete set of ROOT codes for data processing and analysis, available on the GitHub platform [32]. As the tracker is not yet operational for data collection at Modane, we are only interested in the part of the simulations with the calorimeter. The PID module was therefore not used in the reconstruction pipeline, and other criteria, described in the following sub-section, were used to select the Cobalt events of interest. A single off-line analysis pipeline has been developed to handle the different output data models of the simulations and real data, in order to ensure the consistency of the analysis.

6.2.4 Signal events selection

We aim to use the two γ's of 1.17 MeV and 1.33 MeV from ^{60}Co β^- decay, to characterise the time resolutions of individual optical modules. Thus, the signal we are looking for is two particles detected in coincidence in distinct optical modules. In order to maximise the signal to background ratio, some selections have been applied on data.

- Trigger criteria:
  in the two calorimeter hits channel, the trigger condition is defined so as one of the two hit has to trigger the low energy (or amplitude) threshold, of 50 keV for the data acquisition. As we look for two calorimeter hits, we set an additional off-line selection events whose two hits passed both the high amplitude threshold, corresponding to approximately 150 keV.

- Coincidence time criterion:
  we define the coincidence time-window by events occurring in a 62.5 ns-long time interval. This allows to avoid accidental coincidence events (interactions of two gammas, produced by different sources, in two optical modules), while

keeping events where two γ particles interact at both ends of the wall. This time-window was set for the data-taking and can be improved for eventual future acquisitions.

- Individual energy selection:
  in Fig. 6.6 is displayed the highest energy deposit as a function of the lowest energy deposit, for simulations with the ^{60}Co source in position 5. The high

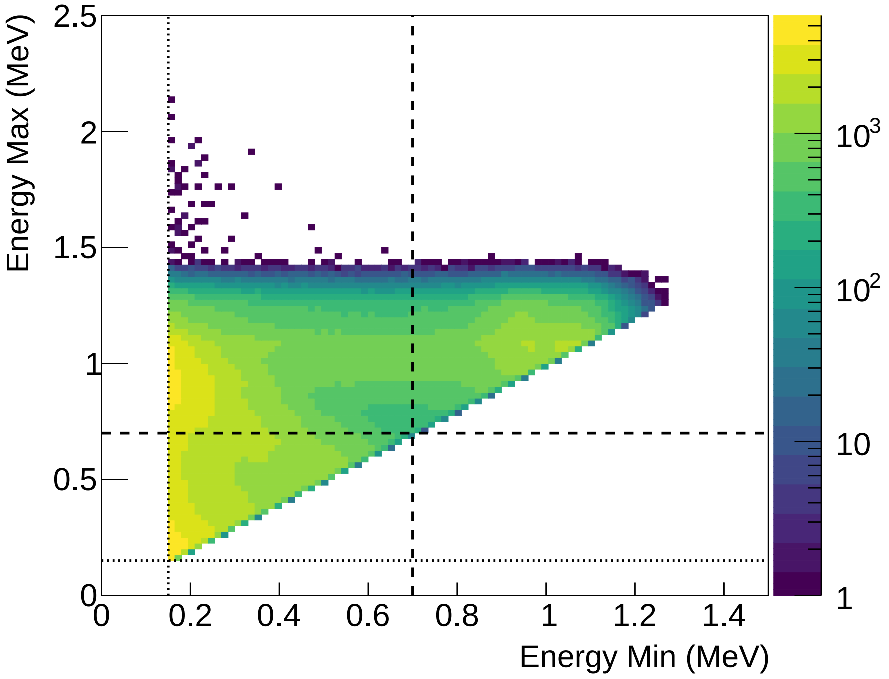

Figure 6.6: Maximal energy with minimal energy, for simulated ^{60}Co events, with source in position 5 (see Fig. 6.5b). High threshold is represented in black dotted line. Dashed lines materialise the individual energy selection.

energy threshold is represented by two black dotted lines. The topology of interest is observable with two hits around 1 MeV. Also, events where two successive Compton interactions of a single photon from Cobalt occur in two different optical modules are characterised by a high energy hit ($\sim$ 0.8 MeV), and a low energy hit ($\sim$ 0.2 MeV). This topology constitutes a background for this analysis because the time difference between the hits has a different distribution. In order to reject them, given the energies of the two interesting ^{60}Co photons, we only select individual calorimeter hit energies greater than 0.7 MeV. This individual energy selection is pictured by two black dashed lines. It naturally highly depends on the calorimeter energy calibration.

- Geometrical selection: with a detector well calibrated in energy, the previous selection is sufficient to prevent double Compton interactions to be selected. But, at the time of the data-taking, the detector was not fully calibrated. The energy of some reconstructed particle hits then might be badly estimated and some background events could pass this energy selection. As such intercations occur predominantly in two close scintillators, we reject topologies where two neighbouring optical modules detect signal in the coincidence window. The detector energy calibration is discussed in Sec. 6.2.5.

These four selections are intended to improve the Cobalt signal to background ratio. The coincidence time selection is only applied to real data, while others are applied both to simulations and real data. Indeed, what we call an *event* does not have the same meaning depending on whether we are talking about simulation or real data. We simulate a given amount of disintegrations at given location(s) of the detector, so the definition of a Monte Carlo event is straightforward, and concepts such as the pile up has no sense. For real data acquisitions, a set of criteria have to be established in order to define what an event is, as the time coincidence window for example.

We remind the signification of selection efficiency ϵ which is

$$\epsilon = \frac{\text{Number of selected events}}{\text{Number of generated events}} \,. \tag{6.5}$$

Selection efficiencies are presented in table 6.1. Significant differences are observed between simulations are real data, mainly due to the energy calibration. Indeed, at the time of the data taking, the gain equalisation and energy calibration were preliminary and had to be improved. Therefore, this statement directly affect the reconstructed energies of calorimeter hits. We address this question in Sec. 6.2.5.

Successive cut-offs	Simulations	Data
High thresold	35.7%	98.0%
Individual energy	17.0%	70.2%
Geometrical	16.5%	61.0%

Table 6.1: Selection efficiencies for simulations and real data.

6.2.5 Energy calibration

The charge collected at each PM divider is correlated to an energy initially deposited inside the scintillator. It is important to provide a robust calibration, allowing to provide a relation between these two observables, for any analysis to be valid. At the time of the data acquisition with the Cobalt source, a complete energy calibration was only provided for data acquisitions taken after the current Cobalt one. Indeed, as the calorimeter was at the beginning of the commissioning phase, several tests were performed, in particular manipulations that required changing the values of the high voltages. The equalisation of gains was therefore not yet implemented, which had an impact on the resolution in terms of energy. In this context, I developped a temporary energy calibration using the data taken with the Cobalt source.

In Fig. 6.7a is displayed charge spectra for two optical modules located in front of the Cobalt calibration source. In order to have a sufficient statistics, only

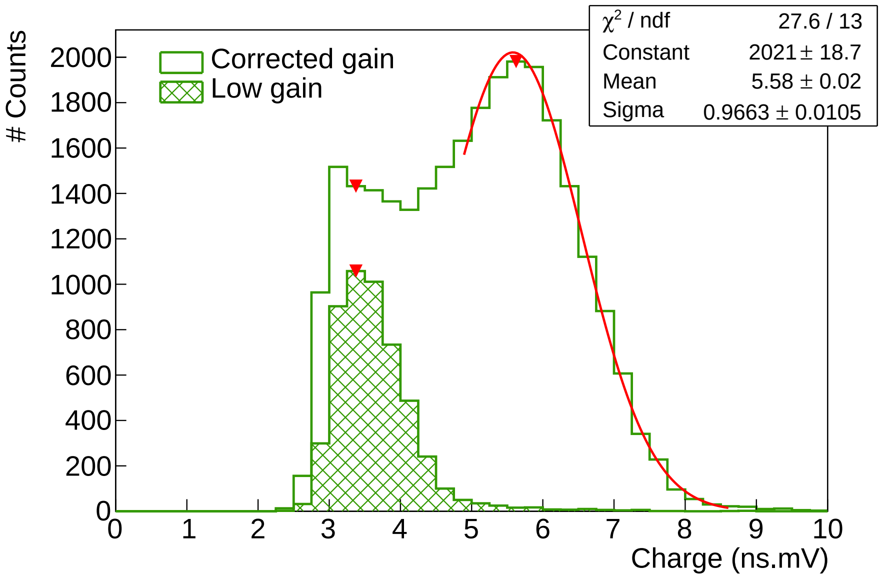

(a) Data acquisition.

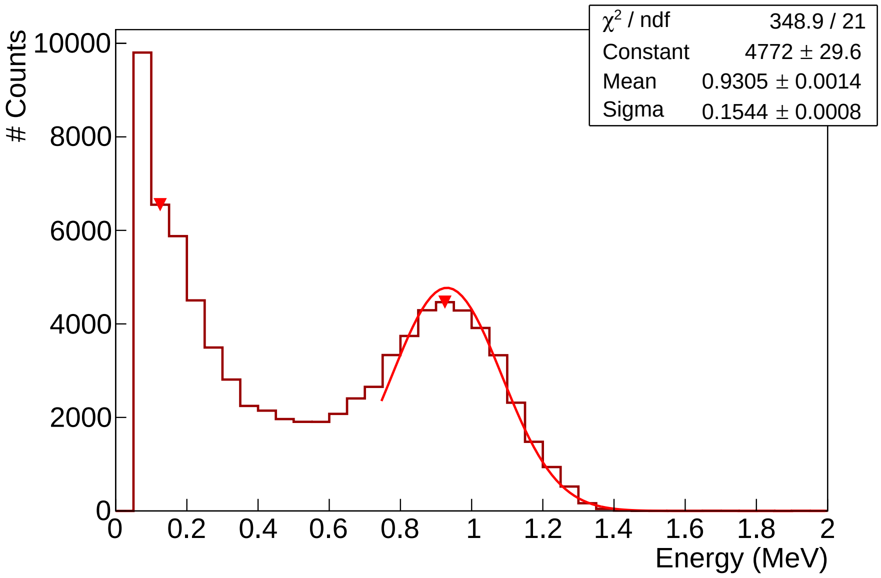

(b) Simulated data.

Figure 6.7: Data acquisition charge (a) and simulated energy (b) spectra. If two peaks are detected, the second one is fitted with a Gaussian. When the OM gain is too low, the lower energy peak, due to a double Compton interaction of a ^{60}Co gamma in two scintillator blocks, is less likely to be detected an the OM is not calibrated.

trigger selection have been applied on data, allowing to select events for which exactly two optical modules triggered (at least one must have triggered the high amplitude threshold). The first peak is mainly populated by double Compton interactions inside the scintillator, and the second by simple Compton interaction of the two Cobalt γ's of interest. For this energy calibration, the second peak is used as the particular point of the distribution. An automatic research of the two peaks is performed and, if exactly two peaks are detected, the second one it fitted with a Gaussian function. This point has been chosen because it is less statistics-dependent than the end point of the distribution. In the figure, an example of an optical module with an appropriate gain is given, and the fit is well-performed. An example of an optical module with a too low gain (because it was under a too low high voltage) is also displayed, and shows only one peak. These kind of distributions were thus no fitted and no energy calibration was provided for them.

The same work is performed on simulated energy distributions for all optical modules. The fits provide an average of the energy location point corresponding to the second peak, of 0.927 ± 0.009 MeV. This work allowed to calibrate 172 optical modules, in total, for the French main wall. An energy spectrum of a successfully calibrated optical module is given in Fig. 6.8 after event selection has been applied. We find the results obtained in the previous sub-section concerning the difference in efficiency between simulations and real data. This will be improved by new data acquisitions that will be taken during the month of November, because all optical modules are now equalised in gain. We also notice that the data spectrum extends at higher energies than simulations, corresponding to the ^{208}Tl background as well as external γ's.

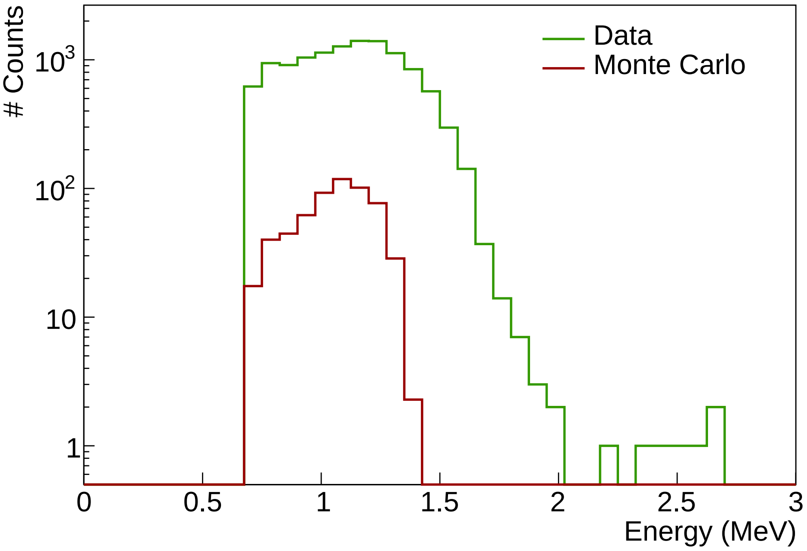

Figure 6.8: Energy spectrum for a calibrated optical module of the French wall, using Cobalt data acquisition. The simulations have been normalised to the source activity and data acquisition time.

Selection efficiencies for each cut-off, after the energy calibration, are given in Tab. 6.2. We notice an improvement at the level of individual energy cut, where the selection efficiency is reduced compared with the previous case using the energy calibration provided by the collaboration.

This is a temporary calibration, only use in the framework of this analysis, and does not replace the more complete one accomplished for later data acquisitions. An amelioration could be brougth with a double fit of the two peaks. Nervertheless,

	Simulations	Data
High thresold	35.7%	94.0%
Individual energy	17.0%	58.0%
Geometrical	16.5%	51.9%

Table 6.2: Selection efficiencies for simulations and real data. Energy calibration with Cobalt data have been applied.

this improvement is not necessary since the gains were not yet aligned. But it will be interesting to try this method again with the new Cobalt data.

6.2.6 Background estimation

The signal for this analysis is composed two γ's of 1.17 MeV and 1.33 MeV, emitted after Cobalt disintegrations. After application of the four selections, it is primordial to estimate and characterise the remaining background in the selected topology, detected by the calorimeter during the data acquisition.

Types of background

Mainly three different types of background can be harmful for this analysis, all pictured in Fig. 6.9.

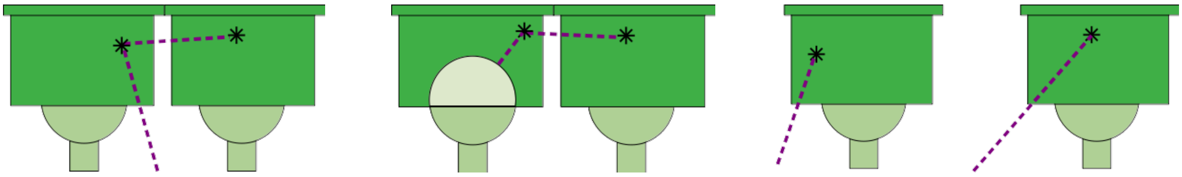
(a) (b) (c)

Figure 6.9: Background types for the Cobalt study. Interactions of photons in scintillators are represented by black stars. (a) Interaction of a single Cobalt photon in two scintillators through double Compton scattering. (b) Interaction of a photon coming from natural radioactive isotopes contamination (PM glass...), through double Compton scattering. (c) Interactions of two uncorrelated photons, coming from the demonstrator outside (natural radioactivity of laboratory rock...), in two scintillator blocks

- Through a double Compton interaction, a single Cobalt γ particle can deposit energy in two scintillator blocks (see Fig. 6.9b). As described in Sec. 6.2.4, the geometrical and individual energy selections have been set up to reject these background events.

- Photons coming from the natural radioactive decay chains of ^{238}U, ^{232}Th and ^{40}K isotopes. Typically, the 2.61 MeV-γ, from ^{208}Tl decay, can interact successively in two scintillators through Compton scatterings and produce high energy events (see Fig. 6.9a). These disintegration can occur in the source foils or in the detector's components (mainly PM glass).

- At the time of the data acquisition, the calorimeter was in commissioning phase, and the iron shielding was not yet installed. Therefore, the calorimeter was not properly protected from external particles, coming from outside the detector (radioactive isotope contamination of laboratory rock). Accidental events where two decorrelated γ particles, can be detected in two scintillator blocks (see Fig. 6.9c). The coincidence time window should avoid these accidental to be selected.

All these three topologies can mimic the Cobalt two-γ's signal.

Estimating the amount of background received by optical blocks during the acquisition is essential to assess our results. In order to characterise the two last types of background (decorrelated from the Cobalt source), an acquisition without the Cobalt calibration source has been performed (see Sec.6.2.3). Unfortunately, be owing to optical modules gain issues, these data are not usable. Therefore, we use the data acquisition taken with the Cobalt source set behind the wall to estimate this background.

Background characterisation

When the Cobalt source is set behind the wall, collected data may contain signal events coming from it as well as background events. Let us assume these background events are dominated by radiocative decays and external γ's, by considering the background coming from double Compton intercations of Cobalt γ's have been efficiently removed by application of the individual energy cut. We choose to modelise the Cobalt data as a linear combination of signal events s and background events b

$$\hat{d} = s + b\,, \tag{6.6}$$

where s and b are thus considered as uncorrelated. The question is how to extract informations about background, using the Cobalt data acquisitions? We remind the Cobalt source was placed at different positions behind the calorimeter wall (Fig. 6.5b, Sec. 6.2.3). We aim to take advantage of those different configurations to reach our goal. In the following, we make use of the positions 2 and 8 for the Cobalt source. Therefore, depending on whether the source is in one of the two positions, some optical modules are *close* to it, others are *far*. More precisely, we consider as *close*, the optical modules that are separated from the source by less than 10 optical modules (i.e. less than half the wall-lenght), the others being *far* from it[1]. Considering that, we distinguish two categories of data, $\hat{d}^{\,\text{close}}$ and $\hat{d}^{\,\text{far}}$, defined as the estimations of data events detected by an optical module when the source is close to, or far from it, respectively. Then, we precise our data modelisation with

$$\hat{d}^{\,\text{close}} = b + s^{\,\text{close}}\,, \tag{6.7}$$

where $s^{\,\text{close}}$ is naturally the number of signal Cobalt events detected by a given optical module for which the distance from the source, D_{source}, is lower than 10.

---

[1] For example, an optical module located on the left (right) of the calorimeter wall, is considered as far from (close to) the source, if the source is in position 8.

In the same way, considering $s^{\,\mathrm{far}}$ as signal events detected by an optical module from which the source is far, we have

$$\hat{d}^{\,\mathrm{far}} = b + s^{\,\mathrm{far}}\,. \tag{6.8}$$

Estimations of $s^{\,\mathrm{close}}$ and $s^{\,\mathrm{far}}$ (respectively noted $\tilde{s}^{\,\mathrm{close}}$ and $\tilde{s}^{\,\mathrm{far}}$) are provided using simulations of ^{60}Co events in positions 2 or 8. Indeed, as we consider the double Compton interaction background as negligible, the amount of signal events received for optical modules far or close from the source can be established with Cobalt simulations. Then, the coefficient α defined as

$$\alpha = \tilde{s}^{\,\mathrm{far}}/\tilde{s}^{\,\mathrm{close}}\,. \tag{6.9}$$

It depends on the distance D_{source} and is found to be $0.05\% < \alpha < 5\%$, meaning that the number of simulated signal events detected by optical modules distant from the source is greatly lower than for close optical modules, for a given source position.

In order to provide a non-biased estimation of b given the data model in Eq. (6.8), we would remove $\tilde{s}^{\,\mathrm{far}}$, estimated through simulations, from $\hat{d}^{\,\mathrm{far}}$, which can be estimated with Cobalt data acquisition. To do so, we display in Fig. 6.10 the number of calorimeter hits, after event selection, counted by each optical module, as a function of the distance to the Cobalt source. The 10 optical modules limit is materialised by a vertical dashed line. Calorimeter hits that occurred in coincidence above and below this limit are displayed both for simulated and real data. Therefore, events where the two hits occur in two optical modules, each

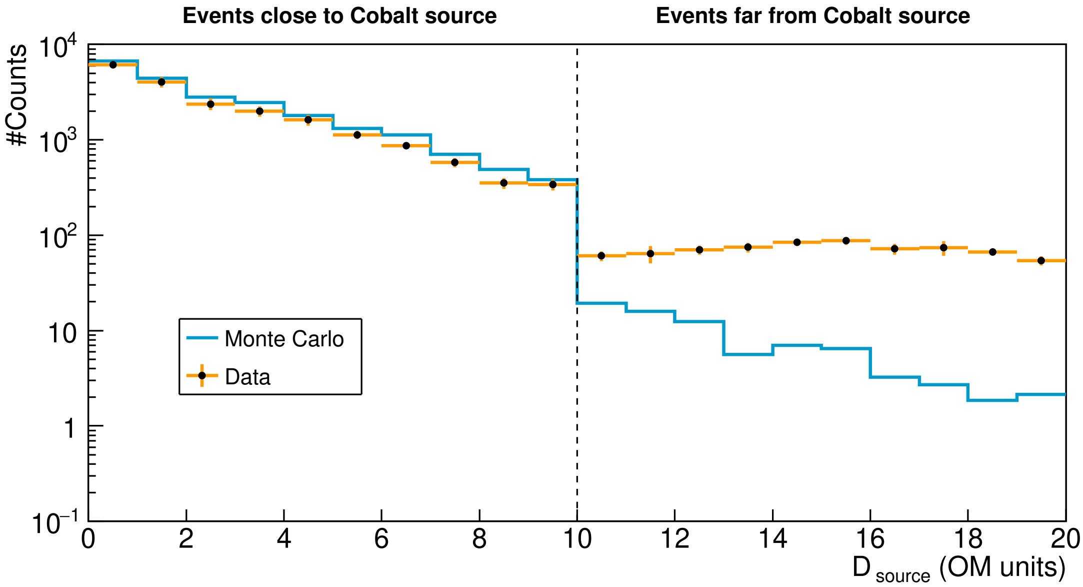

Figure 6.10: Number of events for pairs of OMs close and far from the source, for real data (orange) and simulated data (blue), as a function the distance to the source (in units of number of OM). The vertical dashed line materialises the distance limit of 10 OMs from the source.

located in one half of the calorimeter, are not represented. This explains the observable gap at the 10 optical modules limit level.

We first focus on simulation results. Calorimeter hits for which $D_{\text{source}} < 10$, represent the estimation of the amount of signal events detected close to the source, $\tilde{s}^{\,\text{close}}$. Similarly, hits for which $D_{\text{source}} > 10$ embed for $\tilde{s}^{\,\text{far}}$, the amount of signal events remaining for optical modules far from the calibration source site. As expected, the number of signal Cobalt events decreases with the distance to the source. Moreover, this decrease is linear, showing the same slope beyond and above the 10 optical modules limit.

Regarding real data acquisition, calorimeter hits for which $D_{\text{source}} < 10$ materialise the number of data events estimation $\hat{d}^{\,\text{close}}$. Apart from slight differences due to the detector efficiency, these data events follow the same linear evolution as signal events with the distance to the source. This leads us to conclude that optical modules close to the source are dominated by Cobalt signal events. Similarly, $D_{\text{source}} > 10$ events stand for $\hat{d}^{\,\text{far}}$. We observe that $\tilde{s}^{\,\text{far}}/\hat{d}^{\,\text{far}} \ll 1$, which is compatible with the α coefficient values, being 5% in the worse case, explaining the few amount of $\tilde{s}^{\,\text{far}}$ events remaining for optical modules far from the source. Moreover, we find that the amount of $\hat{d}^{\,\text{far}}$ events is globally stable with the distance to the source, which confirms the assumption made that, at such distances from the source, radioactive contaminant decays and external γ's interactions dominate the background contribution and are decorrelated from the Cobalt source. Therefore, for a 25 minutes run, each optical module detects around 10^2 external background events.

To sum up these results, calorimeter hits for optical modules close to the Cobalt calibration source are, for the most part, signal events. Besides, hits occurring far from the source are predominantly background events. As we moved the source in different positions, we have access to the estimation of background rate $\hat{b}$ for each optical module (when the source is far), and to the estimation of $\hat{s}$ (when the source is close). Therefore, we can compute the signal to background ratio, as a function of the distance to the Cobalt source, displayed in Fig. 6.11. The number of signal events in each optical module depends on the distance to the source, which is not the case for the number of background events, explaining the decreasing of S/B with D_{source}. For this reason, the distribution stabilises at high D_{source} ($\sim$ 8 OM units) as these optical modules are more sensitive to the flat background contribution than those right in front of the source.

To summarise, in this subsection, we gave informations on background events for the whole French wall, using data taken with the Cobalt source set at different positions. We confirmed our assumption that the more one optical block is far from the source, the less it detects γ particles emitted after Cobalt disintegrations, then the more the signal to background ratio decreases.

6.2.7 Determination of the individual timing resolution of each optical module

The final goal of this analysis is to determine σ_t, the time resolution of optical modules. As displayed in Fig. 6.4, the two photons of ^{60}Co are emitted in

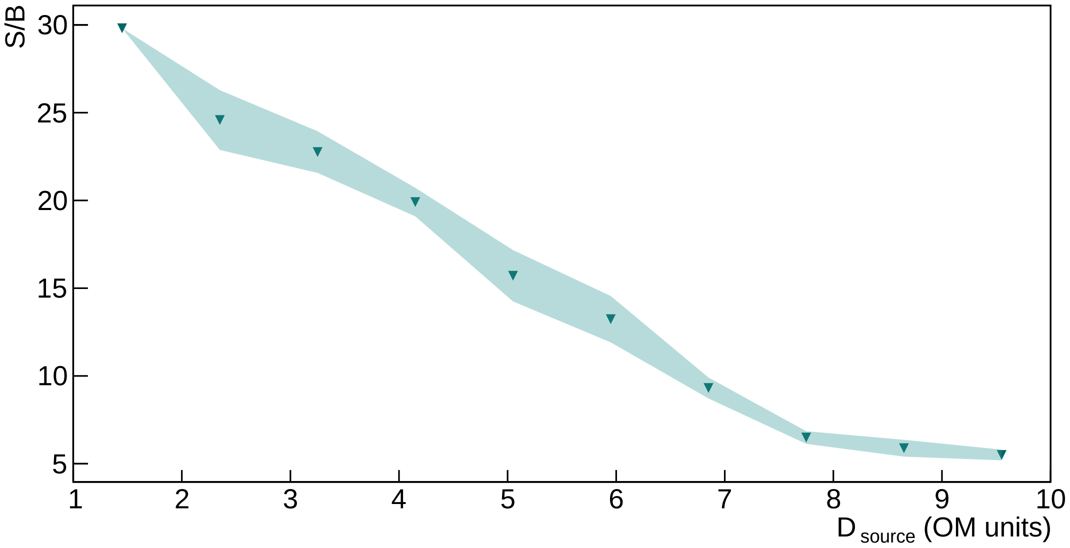

Figure 6.11: Signal to background ratio for each optical module, as a function of the distance to the Cobalt source.

coincidence compared with the time resolution expected for SuperNEMO. The selections described in Sec. 6.2.4 aim to maximise the signal to background ratio, the signal being the detection of two γ's interacting in two different optical modules.

Time difference distributions

The two γ's, travelling at speed of light in air, reach the two optical modules at two different times t_i^γ. These time-of-flights are defined from the sampling of the collected charge, using the CFD method described in Chapter 5. These topologies are likely to happen for all combinations of pairs of optical modules. Therefore, we can construct a Δt^{pair} distribution for each pair of optical module, defined as the time difference between two calorimeter hits $\Delta t^{\text{pair}} = t_A^\gamma - t_B^\gamma$. The two time-of-flights t_A^γ and t_B^γ are corrected from the time offset determined in the precedent Chapter 5, due to the signal travelling inside coaxial cables and to the FEBs time offsets. For a given pair, one of the two optical module is chosen as reference, here A.

In Fig. 6.12 is presented an example of a Δt^{pair} distribution, for a given pair of optical modules, both for the simulated and real data, with the Cobalt source set in position 5. The two distributions present different behaviours in terms of means and standard deviations. This can be explained by two distinct reasons. Firstly, as exposed in Sec. 6.2.1 the simulation are processed with perfect optical modules in terms of time-of-flight measurement. It is thus expected that the standard deviation is higher for real data than for simulations. Even though the case presented is just an example for a given pair of optical modules, this is a general result for all pairs. These different standard deviations are going to be used to determine the σ_t contribution to time measurement uncertainty. Secondly,

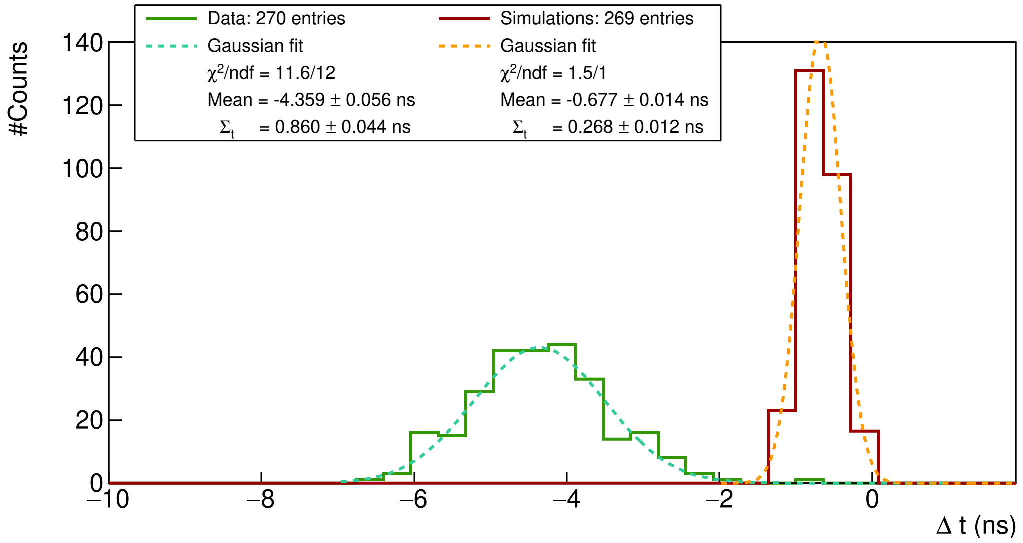

Figure 6.12: Δt^{pair} distributions for real data (green solid line) and simulated data (dark red solid line). Two Gaussian fits (dotted line) are displayed and fit parameters are given in the legend box. The two distributions do not have the same mean because optical modules are not aligned in time. However, this does not disturb the time resolution measurements.

we notice the mean of the real data distribution is shifted towards negative values. This is induced by a systematic time delay of particle time-of-flight value for real data. This result is observed for all pairs of optical modules. As the time-of-flights are corrected from the coaxial cables and FEBs time offsets, this difference could be caused by a difference between simulated and real location of the ^{60}Co source. Moreover, the shift of the mean could also be the consequence of an incorrect energy calibration, that can lead to the selection of background events such as double Compton interactions in two successive optical modules. The average time-of-flight difference for such background events is different from that for signal events, and therefore their accidental selection could be the cause of the observed discrepancy.

Such Δt^{pair} distributions are defined for each pair of optical modules detecting events in coincidence. The least square method is used to fit the distributions, which minimises the difference between the measured value and the fitted value. A mean and a standard deviation is then defined for each pair of optical module whose fitted data has $\chi^2/\text{dof} < 4$. Therefore, due to a lack of statistics, some distributions cannot be fitted properly, and are rejected by the algorithm. At the end, each pair of optical module whose Δt^{pair} distribution fit is selected is characterised by the mean and standard deviation of its corresponding Δt^{pair} distribution. The standard deviation, noted as Σ_t, is called *coupled time uncertainty* and corresponds to the uncertainty on time measurement for this peculiar pair of optical module.

Coupled time uncertainties

The data acquisition was taken with 254 optical modules from French wall instead of 260: at this time three optical modules where out of order, and three photomultipliers whose gain were too low are removed from the analysis. Moreover, in the framework of this study, we intend to characterise timing resolution of 8 inches optical modules only. At the end 214 optical modules were considered, representing more than 2×10^4 different possible combinations of pairs.

With this method, we succeed to provide Σ_t values for 26% of pairs of optical blocks for real data, against 87% for simulations. This difference is due to a lack of statistics for real data. In Fig.6.13 is displayed the number of characterised optical blocks, with the distance between the reference block and the ^{60}Co source, in OM units. The more an optical module is far from the source, the less likely the fit successes. Moreover, for a given distance from the source, the amount of characterised optical module is lower for the real data case than for the simulated one, explaining the lower amount of provided Σ_t values for real data.

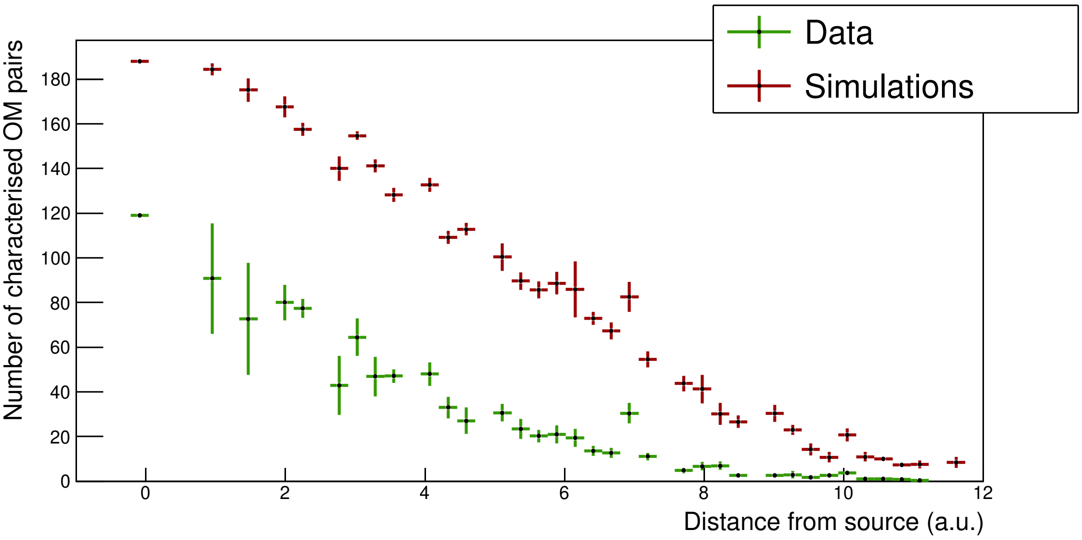

Figure 6.13: Number of characterised OM pairs, as a function of the distance between reference OM and source.

We presented results on the uncertainty on time measurement for pairs of optical module, Σ_t. However, we are interesting in providing such values, independently for each optical modules. Therefore, in the following, we present the algorithm we used to provide individual σ_t values, for each individual optical module.

Decoupling the Σ_t uncertainties

The Σ_t values that have been determined are defined for pairs of optical modules and can therefore be expressed in terms of the individual time resolutions for each module. In order to explain the different steps of the algorithm used to decorrelate these Σ_t, let's take an example of three optical modules having detected, two by two, coincidental events. For each of these optical modules, a Σ_t value can be determined, which is a linear combination of the other two as :

$$\begin{aligned}(\Sigma_t^{0,1})^2 &= \frac{(\sigma_t^0)^2}{\bar{E}_0} + \frac{(\sigma_t^1)^2}{\bar{E}_1}\\ (\Sigma_t^{0,2})^2 &= \frac{(\sigma_t^0)^2}{\bar{E}_0} + \frac{(\sigma_t^2)^2}{\bar{E}_2}\\ (\Sigma_t^{1,2})^2 &= \frac{(\sigma_t^1)^2}{\bar{E}_1} + \frac{(\sigma_t^2)^2}{\bar{E}_2}\,,\end{aligned} \tag{6.10}$$

where $\bar{E}_i$ is the averaged energy measured by the optical module i, and σ_t^i is its individual time uncertainty, so-called *decorrelated time uncertainty*, the quantity we are seeking to determine. Consequently, determining the three individual time resolutions is equivalent to solving this set of equations, and thus diagonalizing the matrix S such that:

$$S = \begin{pmatrix} \bar{E}_0^{-1} & \bar{E}_1^{-1} & 0 \\ \bar{E}_0^{-1} & 0 & \bar{E}_2^{-1} \\ 0 & \bar{E}_1^{-1} & \bar{E}_2^{-1} \end{pmatrix}. \tag{6.11}$$

Once this diagonalisation is carried out, each decorrelated σ_t can be expressed in terms of the three Σ_t.

In practice, this has to be done for all the optical modules for which the Δt^{pair} distribution fit has provided a Σ_t value. With this in mind, the Σ_t values are sorted by order of the number of coincidental events. The work presented above is therefore applied to the first trio of this list. Then the next trio is selected, etc... It is obvious that, when an optical module has detected events in coincidence with more than two other optical modules, then it belongs to more than one trio. Thus it is selected several times to participate in the decorrelation process of several trios. Each optical module can then have many decorrelated σ_t values. The mean of these values, for a given optical module, then represents the final value of σ_t which will be associated to it. The variance of the σ_t is an aspect which is discussed later.

6.2.8 Improvement of the method

- plus de stat (format de fichiers)
- implémenter les corrections en temps
- estimer la variance

6.2.9 Conclusion

- il fauddrait au moins tenir compte du bdf qui est les decays de la source
- il nous faut des simus bkg
- il nous faut un run bkg

- ça marche bien
- 5 inches
- il faudrait refaire une manip avec PMs alignés
- On aurait pu décorréler les sigmas en utilisant toutes les combinaisons possibles, mais il aurait fallu faire masse de simus pour déterminer les covariances
- si on a mal rejeté le bdf 1gamma à cause de la mauvaise calib en énergie, alors on peut avoir une distribution non centrée en zéro qui élargi la distribution delta t et dégrade les résultats finaux.

6.3 The Light Injection System

6.3.1 Light injection system commissioning

In the LI system design, the SuperNEMO demonstrator has been segmented in 10 areas. Each area receives light from one given LED

Primary/secondary Each LED lights Group LEDs/area

6.3.2 Time resolution of optical modules

Bibliography

[1] M. Agostini et al. Probing majorana neutrinos with double-β decay. *Science 365*, 1445, 2019.

[2] S.I. Alvis et al. Search for neutrinoless double-beta decay in ^{76}ge with 26 kg-yr of exposure from the majorana demonstrator. *Phys. Rev. C*, 100, 2019.

[3] O. Azzolini et al. First result on the neutrinoless double-β decay of ^{82}Se with cupid-0. *Phys. Rev. Lett.*, 120:232502, Jun 2018.

[4] C. Alduino et al. First results from cuore: A search for lepton number violation via $0\nu\beta\beta$ decay of ^{130}Te. *Phys. Rev. Lett.*, 120:132501, Mar 2018.

[5] J. B. Albert et al. Search for neutrinoless double-beta decay with the upgraded exo-200 detector. *Phys. Rev. Lett.*, 120:072701, Feb 2018.

[6] A. Gando et al. Search for majorana neutrinos near the inverted mass hierarchy region with kamland-zen. *Phys. Rev. Lett.*, 117:082503, Aug 2016.

[7] Chopra A. C0 commissioning results. Internal presentation, 2015.

[8] Cerna C. Tracker review conclusions. Internal presentation, 2014.

[9] S. Clavez. *Development of reconstruction tools and sensitivity of the SuperNEMO demonstrator*. PhD thesis, Université Paris Sud, 2017.

[10] Garrido X. Bongrand M. Hamamatsu 8" pmt test in magnetic shield. Internal presentation, 2014.

[11] Loaiza P. Source foils measurement with bipo. Internal presentation, 2017.

[12] Perrot F. Radiopurity measurements for 8" pmts and preliminary budget for the sn demonstrator. Internal presentation, 2017.

[13] et al Arnold R. Technical design and performance of the nemo3 detector. *Nucl. Instrum. Meth. A*, pages 79–122, 2005.

[14] Xin Ran Liu. Radon mitigation strategy and results for the supernemo experiment. IoP APP / HEPP Conference, 2018.

[15] A. Huber. *Recherche de la nature du neutrino avec le détecteur SuperNEMO : Simulations optiques pour l'optimisation du calorimètre et performances attendues pour le ^{82}Se.* PhD thesis, Université Bordeaux, 2017.

[16] R. Arnold et al. Probing new physics models of neutrinoless double beta decay with supernemo. *Eur. Phys. J. C*, 2010.

[17] Tretyak V.I. Ponkratenko O.A. and Zdesenko Yu.G. The event generator decay4 for simulation of doublebeta processes and decay of radioactive nuclei. *Phys. At. Nucl.*, 63:1282–1287, Jul 2000.

[18] R. Arnold et al. Results of the search for neutrinoless double-β decay in ^{100}mo with the nemo-3 experiment. *Phys. Rev. D*, 2015.

[19] Gomez-Cadenas et al. Physics case of supernemo with ^{82}se source. Internal presentation, 2008.

[20] R. Arnold et al. Final results on ^{82}se double beta decay to the ground state of ^{82}kr from the nemo-3 experiment. *Eur. Phys. J. C*, 2018.

[21] Cousins D. Feldman G. A unified approach to the classical statistical analysis of small signals. *Phys.Rev.*, pages 3873–3889, 1999.

[22] J. Kotila and F. Iachello. Phase-space factors for double-β decay. *Phys. Rev. C*, 85:034316, Mar 2012.

[23] Dong-Liang Fang, Amand Faessler, Vadim Rodin, and Fedor Šimkovic. Neutrinoless double-β decay of deformed nuclei within quasiparticle random-phase approximation with a realistic interaction. *Phys. Rev. C*, 83:034320, Mar 2011.

[24] A. Chapon. *Mesure des processus de double désintégration bêta du Mo vers l'état excité 0_1^+ du Ru dans l'expérience Nemo3, Programme de R&D SuperNEMO : mise au point d'un détecteur BiPo pour la mesure de très faibles contaminations de feuilles sources.* PhD thesis, Université Caen Basse-Normandie, 2011.

[25] Snow S. A magnetic field map for the tracker. Internal presentation, 2015.

[26] A. Pin. *Recherche de la nature du neutrino via la décroissance double bêta sans émission de neutrinos. Caractérisation et optimisation du calorimètre SuperNEMO et impact sur la recherche de la décroissance du 82Se Développement du premier prototype LiquidO.* PhD thesis, Université Bordeaux-Gradignan, 2020.

[27] A. H. Wapstra G. Audi. The 1995 update to the atomic mass evaluation. *Nucl. Phys. A*, 595:409–480, feb 1995.

[28] R. Arnold et al. Measurement of the $2\nu\beta\beta$ decay half-life of ^{150}nd and a search for $0\nu\beta\beta$ decay processes with the full exposure from the nemo-3 detector. *Phys. Rev. D*, 94, oct 2016.

[29] Estar database (nist). http://physics.nist.gov/PhysRefData/Star/Text/ESTAR.html.

[30] Xcom database (nist). http://physics.nist.gov/PhysRefData/Xcom/html/xcom1.html.

[31] Nucleid database.

[32] My github page. https://github.com/girardcarillo.